



HAL
open science

Observation of three-dimensional trampoline-like behavior in an ultra-light elastic metamaterial

Nikhil Jrk Gerard, Mourad Oudich, Zhenpeng Xu, Desheng Yao, Huachen Cui,
Christina Naify, Alec Ikei, Charles Rohde, Xiaoyu Rayne Zheng, Yun Jing

► **To cite this version:**

Nikhil Jrk Gerard, Mourad Oudich, Zhenpeng Xu, Desheng Yao, Huachen Cui, et al.. Observation of three-dimensional trampoline-like behavior in an ultra-light elastic metamaterial. *Physical Review Applied*, 2021, 16 (2), pp.024015. <10.1103/PhysRevApplied.16.024015>. <hal-04981025>

HAL Id: hal-04981025

<https://hal.science/hal-04981025v1>

Submitted on 6 Mar 2025

HAL is a multi-disciplinary open access archive for the deposit and dissemination of scientific research documents, whether they are published or not. The documents may come from teaching and research institutions in France or abroad, or from public or private research centers.

L'archive ouverte pluridisciplinaire **HAL**, est destinée au dépôt et à la diffusion de documents scientifiques de niveau recherche, publiés ou non, émanant des établissements d'enseignement et de recherche français ou étrangers, des laboratoires publics ou privés.



Distributed under a Creative Commons CC BY-NC-ND 4.0 - Attribution - Non-commercial use - No
Derivative Works - International License

Observation of three-dimensional trampoline-like behavior in an ultra-light elastic metamaterial

Nikhil JRK Gerard^{1,2}, Mourad Oudich^{1,2,3}, Zhenpeng Xu⁴, Desheng Yao⁴, Huachen Cui⁴,
Christina J Naify⁵, Alec Ikei⁵, Charles A Rohde⁵, Xiaoyu (Rayne) Zheng^{5,*} and Yun Jing^{1,2,†}

¹Graduate Program in Acoustics, The Pennsylvania State University, University Park,
Pennsylvania, 16802, USA

²Department of Mechanical and Aerospace Engineering, North Carolina State University,
Raleigh, North Carolina 27695, USA

³Institut Jean Lamour, Université de Lorraine, CNRS, Nancy, 54000, France

⁴Department of Civil and Environmental Engineering and Mechanical and Aerospace
Engineering, University of California, Los Angeles. California 90095, USA

⁵U.S. Naval Research Laboratory, Code 21760, Washington, DC 20375, USA

*rayne@seas.ucla.edu ; †yqj5201@psu.edu

Abstract

Elastic metamaterials possess bandgaps, or frequency ranges that are forbidden to wave propagation. Existing solutions for impeding three-dimensional (3D) wave propagation largely rest on high-volume fractions of mass inclusions that induce and tailor negative effective density based local resonances. This study introduces a class of elastic metamaterials that achieve low frequency bandgaps with a volume fraction as low as 3% (mass density as low as 0.034 g/cm^3). The working of the proposed design hinges on a 3D trampoline-like mode behavior that gives rise to wide, omnidirectional, and low frequency bandgaps for elastic waves despite very low mass densities. Such a 3D trampoline effect is derived from a network of overhanging nodal micro-architectures that act as locally resonating elements which give rise to bandgaps at low frequencies. The dynamic effective properties of the metamaterial are numerically examined, which reveal that the bandgap associated with the trampoline effect is resulted from a negative effective modulus coupled with a near-zero yet positive effective density. The experimental characterization is then made possible by fabricating the metamaterial via a light-based printing system that is capable of realizing micro-architectures with overhanging micro-features. This design strategy could be useful to applications where simultaneous light weight and vibration control is desired.

I. INTRODUCTION

Controlling wave propagations via designed structures is essential in sound attenuation and vibration mitigation. Periodic architectures potentially offer bandgaps or frequency ranges where wave propagation is forbidden. However, relying on periodic phononic crystals with Bragg scattering alone, is far from being practical in managing low frequency vibrations as long wavelengths require impractically large features. Elastic metamaterials offer the unique advantage of controlling acoustic [1,2] and elastic waves [3,4] owing to their ability of tailoring bandgaps at

wavelengths much larger than their periodicities. These metamaterials are typically constructed by inserting heavy mass at the core of the periodic scaffold, which induces a local resonance phenomenon [5–15]. Via tailoring the lattice geometry and stiffness of the mass inclusions, a range of low frequency and wide bandgaps can be generated and tuned. This intuitive design concept, however, comes at the cost of significantly added masses, rendering them impractical when scaled up for engineering applications. While a few alternative methods [3,16–18] have been demonstrated based on periodic arrangement of pillars and hole arrays on a plate that achieve low frequency bandgaps, these designs are only capable of operating in the case of 2D plate (Lamb) waves. Achieving 3D omni-directional low frequency bandgaps still requires large mass inclusions. Developing lightweight three-dimensional metamaterials for low frequency vibration isolation from all directions, thus, remains elusive.

In this work, we introduce a class of ultralow density elastic metamaterials that exhibit a three-dimensional trampoline-like resonance and can achieve wide-band omnidirectional vibration attenuation at low frequencies. The high porosity (exceeding 95% void space) of our micro-lattice enables a mass density that is as low as 0.034 g/cm^3 . The design features a network of low stiffness nodal structures within an array of overhanging micro-unit cells that facilitate a pair of distinct local resonance-based bandgaps at relatively low frequencies. The proposed metamaterial is analyzed via a theoretical lumped model and its dynamic properties are numerically investigated to show that the 3D trampoline effect gives rise to a bandgap that is associated with negative bulk modulus and near-zero yet positive effective density over a wide frequency range. This is quite different from the BGs seen in conventional 3D elastic metamaterials that rely entirely on heavy masses to induce negative effective density based local resonances. The fabrication of the ultralight prototype is enabled by a large area projection micro-stereolithography platform capable of

micro-scale overhanging 3D features that make up the isotoxal auxetic topology of the proposed metamaterial. The observed low frequency bandgaps (BGs) in these ultralow density metamaterials decouples the previous mass density and feature size trade-off for elastic metamaterials and offers insights on the dynamic behavior of micro-lattice-based metamaterials for applications in vibration control and energy harvesting for aerospace, automotive and civil infrastructural systems.

II. UNIT CELL DESIGN

Three-dimensional architected metamaterials represent a promising class of low-density materials with micro-lattice topologies that offer numerous advantages in structural [19,20], thermal [21] and energy absorption [22,23] properties. These metamaterials include octet-truss, tetrakaidecahedron, kagome and auxetic lattices that comprise open cellular topologies with nodal connectivity that can be additively manufactured and can display high strength and tailorable energy absorption at a fraction of the weight of the solid material.

Auxetic lattices are those that exhibit a static negative Poisson's ratio by counter-intuitively increasing (or decreasing) in the lateral direction when they are subject to a tensile (or compressive load) [24–28]. These were put forward a couple of decades ago and have ever since been investigated for their usefulness in various biomedical, aerospace and textile applications, owing to their compressibility and energy absorption capabilities. Efforts have also revealed that in addition to the conventional auxetic geometries, auxeticity can also be induced via chirality [29–31], rotating units [32,33] and random or entangled topologies [33,34]. Auxetic micro-lattices are hence excellent candidates for multiple functionalities and some recent studies have also engineered micro-lattices to possess bandgaps for elastic waves alongside auxeticity. However, majority of these works are theoretical and have been constrained to 2D wave propagation [35–37], and the few designs proposed for 3D [8,38,39] still rely on heavy masses in the core of the unit cells, to induce negative density-based bandgaps. This study on the other hand, proposes

a 3D auxetic micro-lattice that possesses a trampoline-like dynamic negative-modulus-based resonance that enables wide bandgaps despite the material being ultra-light. This is done by devising a 3D cubic auxetic unit cell that is inspired from a re-entrant two-dimensional auxetic unit cell [40]. The reported micro-lattice consists of a network of 3D isotoxal unit cells (shown in **Fig. 1(a)**). Each unit cell comprises 30 solid cylindrical rods of the same diameter and intrinsic material. Among these, 24 inner rods make up 3 mutually perpendicular isotoxal square stars in the xy , yz , and zx planes, while 6 slightly smaller outer rods connect the unit cell to its adjacent neighbors. As illustrated in **Fig. 1(b)**, the defining dimensions of this geometry are p , d , a , and θ , where p and a refer to the periodicity and the distance between the vertices of the squares respectively, while d denotes the diameter of the rods and θ is the angle that the inner rods make with the vertical normal. The numerical results in **Fig. 5** of **Appendix A**, illustrate the auxetic behavior of the sample as a function of θ and d/p . The intrinsic material properties that were employed for this simulation and for the ones that follow, were consistent with that of the base material that was later employed for the fabrication of the prototype (Young's Modulus, $E = 512$ MPa; density, $\rho = 1.1$ g/cm³; intrinsic Poisson's ratio, $\nu = 0.3$).

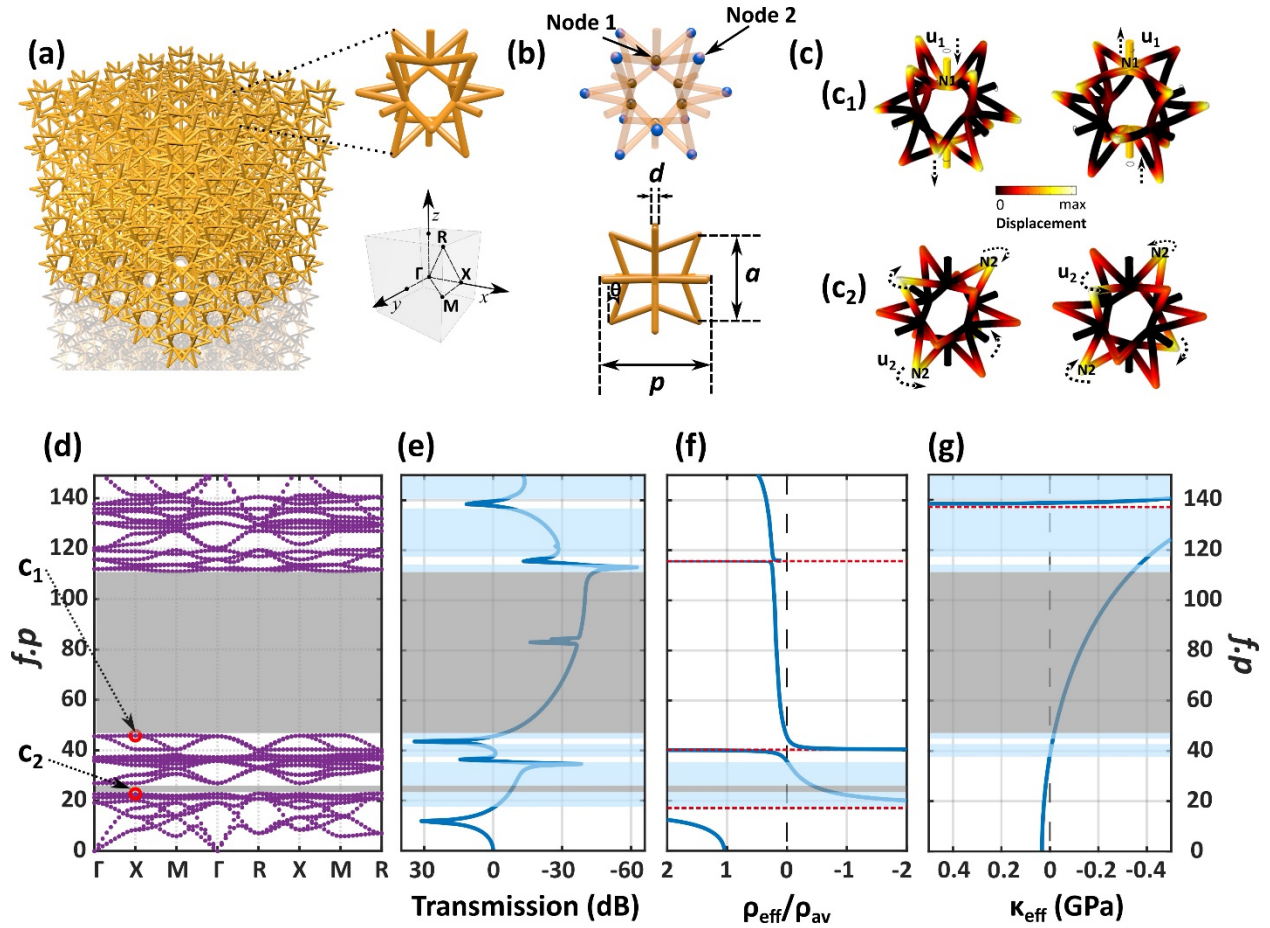


Figure 1. (a) Ultra-light micro-lattice-based elastic metamaterial composed of periodic auxetic building blocks (top-right) and the directions of the irreducible Brillouin zone (IBZ), for the simple cubic unit cell (bottom-right). (b) (Top) Nodes 1 and 2 of the unit cell, denoted by the black and blue spheres, respectively. (Bottom) Dimensions of the unit cell: p is the periodicity, and a is the distance between the vertices of the isotaxal squares, θ is the angle between the outer edges of the isotaxal square stars and the vertical. (c) Snapshots of the resonance modes that give rise to bandgaps (BGs). u_1 and u_2 denote the longitudinal and torsional displacement of the nodes 1 (N1) and 2 (N2) respectively. (d) Normalized band structure for the simple cubic auxetic unit cell along the different directions of the IBZ, for $\theta = 20^\circ$, $a = 0.8p$, and $d = 0.060p$. c_1 and c_2 are the modes at the X point (red circles) on the lower edges of the BGs. (e) Longitudinal wave transmission in dB, for propagation in the ΓX direction. Frequency dependent (f) effective density, ρ_{eff} , and (g) effective bulk modulus, κ_{eff} . The dashed red lines in (f) and (g) indicate sudden jumps in ρ_{eff} and κ_{eff} , from positive to negative values and vice versa. The regions in grey denote complete BGs, while those shaded blue indicate the BGs associated with longitudinal waves only.

III. ELASTIC WAVE DISPERSION

The elastic wave dispersion through the micro-lattice was then systematically studied by calculating its band structure and dynamic effective properties. Eigenfrequency simulations were first carried out on a single unit cell of the metamaterial with Floquet periodic boundary conditions. Here, the parameter a was fixed to $0.8p$, d , at $0.06p$ and the value of θ was chosen to be 20° . The band structure for a sample of these dimensions is shown in **Fig. 1(d)** and indicates that two complete BGs of fractional bandwidths, 16.1% and 82.8%, were observed (regions in shaded grey) in the normalized frequencies ($f.p$) ranging from 22.9 to 26.9 and from 45.95 to 110.95, respectively. The occurrence of such low frequency BGs can be attributed to local resonances that arise as a result of nodes 1 and 2 (shown in **Fig. 1(b)**) playing the role of two distinct masses and springs. This is in stark contrast to conventional 3D micro-lattices [19,41,42] and elastic metamaterials [7–15] where all the vertices of the lattice are identical and therefore only contain one type of homogeneous nodal structure as illustrated in **Appendix B**. In this case, however, the unit cell topology reveals two distinct types of nodal structures as shown in **Fig. 1(b)**. Here, node 1 is attached to 5 rods in total (4 inner and 1 outer), while node 2 is attached only to 2 inner rods. This distinction allows for the existence of the two very different local resonance modes shown in **Figs. 1(c₁)** and **(c₂)** and in turn give rise to the two distinct BGs in **Fig. 1(d)**. The nodal structures comprise local mass-spring systems that can be analyzed via a lumped mechanical model (**Appendix C**), with their masses at nodes 1 and 2, i.e., m_1 and m_2 , and the effective stiffnesses of the interconnecting springs, K_1 and K_2 , obtained by calculating the reaction force and displacement under a global excitation (**Figs. 7, 8, Eqns. C1, C5, C13 and C14**). It was found that K_1 is over two orders of magnitude higher than K_2 . For an example of the geometric parameters chosen here, K_1 has a stiffness of 150 kN/m, while K_2 is 500 N/m. Since the frequency of resonance is directly

proportional to the square root of the stiffness, this would explain why (1) the BG associated with node 2 can occur at a very low frequency even with a small mass density (0.034 g/cm^3); (2) the BG associated with node 1 would occur at a higher frequency than that associated with node 2, due to its larger stiffness. **Figs. 1(c₂)** and **(c₁)** show the mode behaviors of the unit cell at the lower edges of the first and second BGs, respectively. **Fig. 1(c₂)** indicates the resonance associated with K_2 since the outer rods that connect to node 1 remain stationary, while the inner rods that connect to node 2 are in torsional oscillation. Similarly, **Fig. 1(c₁)** indicates the resonance associated with K_1 that occurs at a higher frequency and therefore corresponds to the case where the inner rods remain stationary while the outer rods experience a high degree of flexibility that allows them to vertically bounce on node 1. The wave behavior observed here is very similar to the motion offered by a trampoline as indicated by the dashed arrows in **Fig. 1(c₁)**. For a better visualization of the aforementioned modes, the reader is referenced to the animation shown in the **Supplemental Material** [53]. Since the geometry of the unit cell obeys cubic symmetry, the mode shape shown here is indicative of the displacement that would exist in the xy and yz planes. Such a distinctive wave-behavior was previously known to exist only in the case of pillared-plates [16,17], where the trampoline-like mode was shown to amplify the effect of the local resonance and therefore increase the width of its associated BG. A unique 3D trampoline behavior that amplified the effect of the local resonance is now seen in a lightweight 3D micro-lattice and enables the second BG of width 82.8%. This mode transcends the requirement for heavy masses or multiple materials employed in 3D elastic metamaterials to induce local resonance [7–15,38,43–45].

To further elucidate the origin behind the aforementioned BGs, frequency domain simulations were then performed by applying a longitudinal excitation on one face of the unit cell and then extracting the dynamic effective properties at the X point of the irreducible Brillouin zone

(IBZ). **Fig. 1(e)** shows the simulation result for the longitudinal wave transmission through the ΓX direction of the metamaterial. This curve clearly illustrates very low transmission in the regions that correspond to the two complete BGs, marked by the shaded grey regions in **Figs. 1(d)** and **(e)**. Additionally, in the case of **Fig. 1(e)**, one can also observe very low transmission in the regions that are shaded blue, owing to the BGs that exist here for longitudinal waves only. The physical properties of the BGs in both the grey and blue regions can be further explained by calculating the frequency dependent density [46], ρ^{eff} , and bulk modulus [47], κ^{eff} . This was done by evaluating the average resultant forces, displacements, stresses, and strains, along each of the unit cell's boundaries and then incorporating them in the formulation shown in **Appendix D**. It must be noted that a longitudinal excitation along the ΓX direction was chosen here as an illustrative example to calculate the dynamic effective properties of the metamaterial. Since the associated BGs are in all directions and for all modes, one could employ this method, for shear elastic modes and for other directions of propagation as well.

Fig. 1(f) shows the result for the dynamic effective density, normalized by the average density of the unit cell, ρ_{av} , and **Fig. 1(g)** shows the curve for dynamic effective bulk modulus as a function of the frequency. It is important to note that the effective density and moduli studied here, are frequency dependent and hence different from the static negative material properties that are conventionally studied in the case of auxetic materials. It can be observed that the narrow BGs at the lower frequencies are due to negative density and positive bulk modulus, while the wider ones at slightly higher frequencies come as a result of negative bulk modulus and positive density. This is true for the complete BGs (marked by the grey regions) as well as for the ones that exist only for longitudinal waves (marked by the blue regions). The wider BG that occurs between $f.p = 45.95$ and 110.95 , corresponds to a region that efficiently couples a large negative effective

modulus with a positive near-zero effective density. The wide-band performance enabled here is in stark contrast to the current state of the art in 3D elastic metamaterials [7–12,14,15,38,43–45], where masses are employed in the unit cells. Although prior studies did not shed light on the dynamic effective properties of the 3D metamaterials, the fact that they rely on heavy masses suggests that the associated BGs are purely based on negative density. The BG associated with the trampoline-like resonance reported here is thus a departure from the status quo and offers an advanced route for 3D vibration control. Additionally, the sudden peaks that lie between any two adjacent BGs in the transmission curve, occur as a result of the effective properties being either both positive or both negative. Such a double negative behavior in an ultra-light metamaterial could also greatly aid applications like negative refraction [48] and super-focusing [49], that have only been realized for 2D elastic wave propagation till date.

IV. BANDGAP TAILORABILITY

Furthermore, the width and frequency ranges of the complete BGs can be conveniently tuned via the geometrical parameters of the unit cell. Altering the geometrical parameters allows for the judicious and simultaneous tailoring of the widths of both the negative density and modulus regions. For instance, **Fig. 2(a)** shows the evolution of two complete BGs as a function of θ , for different values of a , while the value of d is fixed at $0.06p$. It can be observed here, that decreasing the value of a increases the frequencies at which these BGs occur. Further, this also lowers the frequency of the mode that exists between the two BGs, thereby increasing the width of the high frequency BG, while reducing that of the lower one. Additionally, when the value of a reaches $0.8p$, the increased length of the inner rods allows for the existence of a lower frequency torsional mode that gives rise to the negative density-based BG that is seen here and is also noted previously in **Fig. 1(d)**. Similarly, **Fig. 2(b)** shows the variation of the two complete BGs as a function of θ ,

for different values of d when the value of a is fixed at $0.8p$. In this case, it can be noted that increasing the value of d would increase the mass of all the struts in unison and not just that of the outer rods. This would hence increase the frequency ranges at which both the BGs occur coherently, without much change to the width of the individual BGs. At much higher values of d/p , however, the negative density-based narrowband BG is replaced by multiple BGs of similar width. In addition to the geometrical parameters, the BGs can also be tailored via the properties of the intrinsic material that is employed for its fabrication. As can be seen in **Fig. 2(c)**, the frequency range of the BG can be considerably increased (decreased) by simply utilizing an intrinsic material that has a higher (lower) Young's Modulus.

From **Figs. 2(a)** and **(b)**, it can be seen that the BG associated with the trampoline mode appears widest when a and d are $0.8p$ and $0.06p$, respectively. These parameters were therefore fixed in order to further investigate the influence that the relative orientation, θ , has on the BG behavior. As seen previously in **Figs. 2(a)**, **(b)** and **(c)**, multiple BGs can be opened and closed in this case as well, by simply tuning the value of θ alone. It must be noted here that the value of θ in this study is considered to lie only between 5° and 40° , so as to ensure that the vertices of the isotoxal stars do not overlap. **Fig. 2(d)** shows the evolution of the complete BGs (shaded grey regions) as a function of θ and the dashed black line denotes the center frequency of the second BG that corresponds to the trampoline mode. It is evident here that the BG of interest would be at its widest and lowest, when $\theta = 20^\circ$. A structure with these optimal dimensions was hence chosen as the candidate for the previous section and for the experimental study that follows.

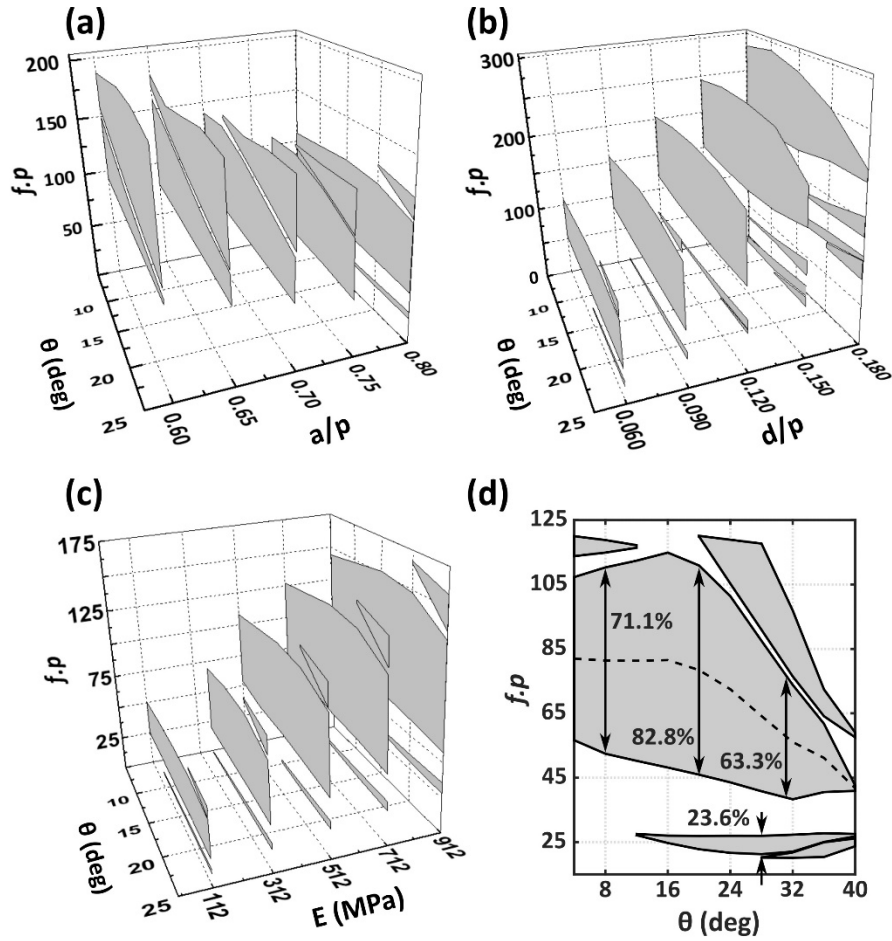


Figure 2. Accessing bandgaps that occur at other frequency ranges and/or with other bandwidths. (a) shows the evolution of the gaps as a function of the geometrical parameters, a/p and θ , when the value of d is fixed at $0.06p$, (b) shows the gaps as a function of d/p and θ , when the value of a is fixed at $0.8p$, (c) shows the gaps evolve as a function of the Young's Modulus, E , and θ , when d and a are fixed at $0.06p$ and $0.8p$ respectively ; (d) The evolution of the BGs (shaded grey regions), as a function θ , for the unit cell where $d = 0.8p$, $a = 0.06p$ and $E = 512$ MPa, where the dashed black line indicates the central frequencies of the widest BG.

Fig. 3 compares the wave attenuation performance of the present metamaterial with the previously reported 3D elastic metamaterials (mass densities and normalized frequencies, $f.p$) and the measured BGs associated with each study were respectively color coded. This chart indicates that our micro-lattice-based design (denoted by the bar in grey) can achieve wide-BGs at low normalized frequencies and simultaneously possess the lowest effective density at a fraction of the density of previous metamaterials.

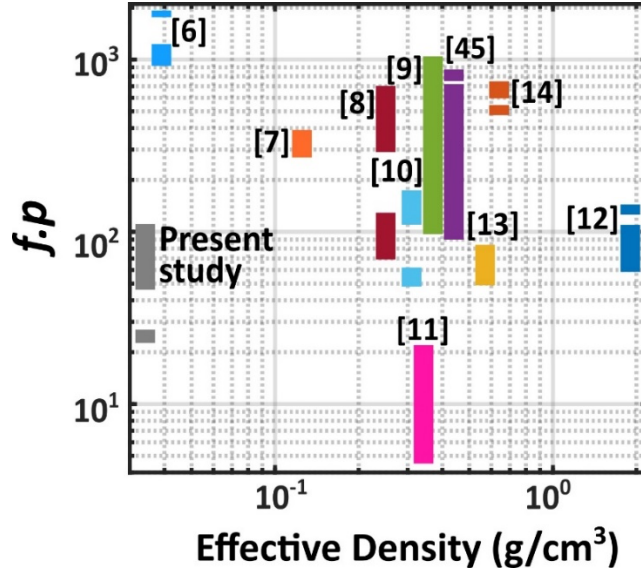


Figure 3. An illustration of the ultra-low effective density that is achieved in the study alongside the wave attenuation performance at small values of normalized frequency ($f.p$), in comparison with the performance of relevant prior works. Each of the references is individually color-coded and the height of the bars denote the regions of $f.p$ where their bandgaps lie.

V. EXPERIMENTAL REALIZATION

The fabrication of our intricate isotoxal based elastic metamaterial was made possible by a high-resolution fabrication technique that is discussed in detail in **Appendix E**. **Figure 9(b)** shows photographs of the as-fabricated samples along three different orientations. These are the (1,0,0), (1,1,0) and (1,1,1) and were chosen to be consistent with the ΓX , ΓM and ΓR directions of the IBZ shown in **Fig. 1(a)**. Although the three samples have the same basic dimensions for d , θ and a , the periodicities of the metamaterial along the ΓX , ΓM and ΓR directions are p , $\sqrt{2}p$, and $\sqrt{3}p$, respectively. Here, $p = 2$ cm, and the widths of the resultant samples were 6 cm, 5.65 cm, and 6.9 cm, and comprised of 3, 2 and 2 units, respectively. In addition to the lattice based micro-structure, the fabricated samples also had plates with a thickness of 3 mm on either side, for the convenience of the experimental characterization.

The transmission measurement through the sample was carried out by placing the GX, GM and GR samples on a measurement platform as shown in **Figs. 4(a), (b) and (c)** respectively. The bottom plate of the sample was connected to a B&K 4809 mechanical shaker that facilitated the longitudinal excitations that served as the input wave. The top plate on the other hand, was connected to a PCB Piezotronics 352C33 accelerometer (100 mV/g) that measured the wave that transmits through the sample and reaches the other side. A schematic of the entire experimental set-up is shown in **Fig. 4(d)** where the accelerometer is connected to an ICP Signal Conditioner (PCV 482C05), that transmits the acquired data to an SRS860 high frequency lock-in amplifier. The lock-in amplifier was controlled by a custom LabView program, such that its internal oscillator is amplified by a B&K 2718 amplifier and in turn used to drive the mechanical shaker. The internal reference frequency of the SRS860 was programmed to cycle from 500 Hz to 10 kHz in 10 steps, the data was sampled with a 10 ms time constant, and an 18 dB low pass filter was applied to enable a high signal-to-noise ratio.

Fig. 4(f) shows the complete band structure for the fabricated samples where $p = 2$ cm and **Fig. 4(e)** denotes the results from numerical simulations that mimicked the experimental platform. In **Fig. 4(e)**, the normalized displacement field for the GX, GM and GR samples are shown for the case where the excitation is applied to the bottom plate (as indicated by the black arrows) and has a frequency that lies within the region of the BG. As can be seen here, when a wave of 4 kHz tries to propagate through the lattice, the trampoline-like behavior facilitates an extremely high wave attenuation by completely reflecting the incident energy. The wave, therefore, does not propagate through more than half a unit cell and enables high wave attenuation through a sample that has a very small number of unit cells (the animation of wave propagation through the lattice clearly illustrates this and can be found in the **Supplemental Material** [53]).

Figs. 4(h) shows the experimentally obtained frequency dependent transmission curves for the ΓX , ΓM and ΓR samples. These are denoted here by the blue, orange, and red lines, respectively. All three curves undergo a sharp decay in transmission at the frequencies between 1.95 kHz and 4.7 kHz and confirms the existence of a BG of width 82.7%, in this frequency range. This is in reasonable agreement with the trampoline-resonance based BG of width 82.8%, that we expect to see between 2.3 kHz and 5.55 kHz, from the numerical results. The shift of this BG to a slightly lower frequency range in the experimental results can be attributed to minor deviations in the stiffness of the intrinsic material. Furthermore, another cause for this shift could be the deviation in the geometrical parameter, θ , that possibly arises due to the weight of the accelerometer that is placed on the top plate of the sample. One could envision that the weight associated with the accelerometer would increase the value of θ in the metamaterial unit cell (see **Fig. 1(b)**). Judging from the plot in **Fig. 2(d)**, increasing the value of θ would decrease the frequency of the second BG, and this is consistent with what is observed in the experiment. Further, the plot in **Fig. 2(d)** indicates that the increase in θ would open a third BG at higher frequencies. This therefore can also explain the dip that is seen at frequencies around 6 kHz, for the measured results but not the bandstructure in **Fig. 4(f)**. To confirm the cause for this deviation, **Fig. 4(g)** shows the numerically calculated frequency dependent transmission through the three samples with corrected values for Young's Modulus, E , and angle, θ (i.e., $E = 415$ MPa instead of 512 MPa, and $\theta = 21^\circ$ instead of 20°) and demonstrate a closer agreement with the experimentally measured results. The material properties that were employed for this calculation and the relevant bandstructure can be found in **Appendix F**.

In both **Fig. 4(g)** and (h), besides the frequencies associated with the complete BGs, low transmission is also observed in the regions where there are BGs for longitudinal waves only. This

is due to the fact that the input excitation here is purely longitudinal, as is the case in the experimental set-up. The low frequency BG of width 16.1%, that exists between 1.13 kHz and 1.35 kHz on the other hand, is quite narrowband and is hence challenging to observe in the experiments. To add to this, the frequency region associated with this narrow-band BG (1 – 1.8 kHz) also possesses BGs for longitudinal waves. This is clearly observed in the numerical results in **Fig. 4(g)** and therefore makes it difficult to differentiate the different narrowband regions of low transmission in the experimental curves as well. However, a considerable dip can be seen in the case of the ΓM and ΓR curves, in the regions between 900 Hz and 1.05 kHz, which reasonably correspond to the negative density-based BG that is expected for this metamaterial. From both the **Figs. 4(g)** and (h), one can also observe that the decay measured in the BG regions is highest in the case of the ΓR sample and lowest in the case of the ΓM sample. This is due to the proportionally different sample lengths in the three cases, with ΓR being the longest and ΓX being the smallest.

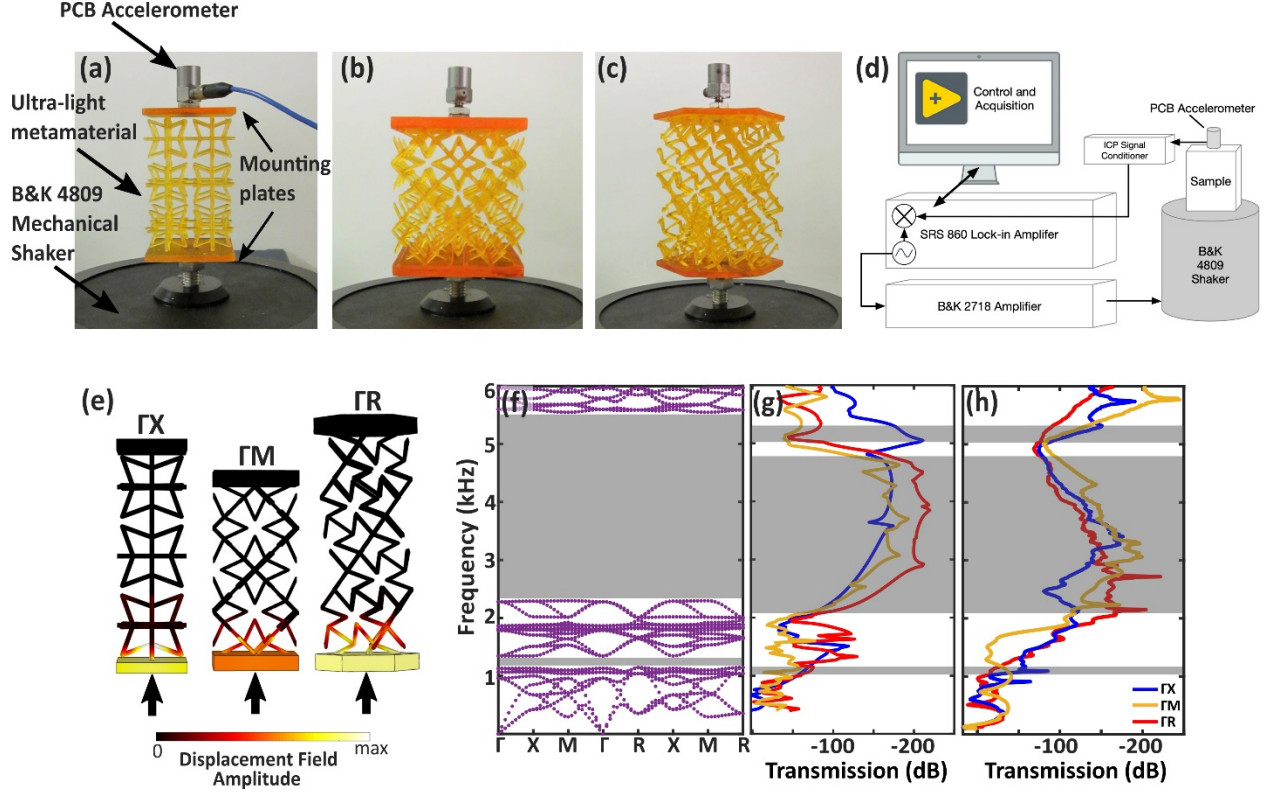


Figure 4. Photograph of the measurement platform with the (a) ΓX , (b) ΓM , and (c) ΓR samples mounted, (d) Schematic of the experimental measurement set-up, (e) Numerical results of the normalized displacement field for the ΓX , ΓM and ΓR samples, for a frequency of excitation of 4 kHz, (f) Bandstructure (in kHz), for the unit cell where $\theta = 20^\circ$, $d = 0.06p$ and $a = 0.8p$, and the material properties were $E = 512 \text{ MPa}$, $\nu = 0.3$, and $\rho = 1.1 \text{ g/cm}^3$ (g) Results from frequency domain transmission simulations through the three samples under consideration with $\theta = 21^\circ$, corrected material properties (shown in **Appendix F**) and an isotropic loss factor of 0.01 (h) Experimentally measured elastic wave transmission (dB) through the ΓX , ΓM and ΓR samples - denoted by the blue, orange, and red curves, respectively. The shaded grey regions in (f) - (h), indicate the BGs.

VI. CONCLUSION

To summarize, we report an ultra-light micro-lattice-based metamaterial that possesses 3D trampoline-like resonant modes and therefore achieves wide-band omnidirectional elastic wave attenuation. A lumped mechanical model was developed to analyze the system theoretically and its dynamic properties were numerically examined to unveil the effective density and modulus that are associated with the 3D trampoline-induced BG. Furthermore, it was demonstrated that the

widths and frequency ranges of the BGs associated with this metamaterial can be conveniently tuned via the geometrical parameters of the micro-lattice. The metamaterial with desirable characteristics was then fabricated by our unique manufacturing capability and experimentally characterized to corroborate the results in our numerical simulations. It was observed here that the trampoline-like mode enables complete wave reflection in the BG region, with a very small number of unit cells. Such a high wave attenuation, accompanied by an ease of tailorability, can be leveraged to further increase the width of the BG (an example that numerically illustrates this in one wave propagation direction can be found in **Appendix G**). In addition to its elastodynamic functionality, the proposed metamaterial also possesses a second order functionality of exhibiting auxeticity or a static negative Poisson's ratio. This would greatly aid applications that demand a marriage of these unrelated yet highly advantageous functionalities. Both the auxetic and elastodynamic performance could also be further enhanced via the use of multiple materials in the micro-lattice [21,50]. In contrast to the existing strategies for vibration attenuation which are heavy and/or relatively impervious, the material introduced here has a 97% porosity and could also allow the co-existence of other functionalities like thermal insulation and airborne sound absorption, that were previously unattainable. Lastly, the tailorability of this design could also be leveraged in the future for adaptive and reconfigurable elastic wave control.

ACKNOWLEDGMENTS

Y. J. acknowledges the startup support from Penn State University. Z. X, D. Y and X. Z thank the Air Force Office of Scientific Research (FA9550-18-1-0299), Office of Naval Research (N00014-18-1-2553), and the National Science Foundation (2001677) for their financial support. C. N, A. I, and C. R. were supported by the Office of Naval Research.

N. J. G., M. O., Z. X., and D. Y. contributed equally to this work. N. J. G. and M. O. performed the design and numerical simulations. Z. X. and H. C. fabricated the samples. D. Y built the theoretical model and helped with mechanical interpretations. C. J. N., A. I., and C. A. R. carried out the transmission experiments. N. J. G., M. O., X. Z., and Y. J. wrote the paper with contributions from all the authors. Y. J., and X. Z. supervised the project.

APPENDIX A: STATIC NEGATIVE POISSON'S RATIO OF THE 3D ISOTOXAL BASED ELASTIC METAMATERIAL

To verify the auxeticity of the proposed metamaterial, static numerical simulations were carried out using the solid mechanics module on COMSOL Multiphysics 5.3(a). A known longitudinal displacement was prescribed on one face of a finite sample made up of $3 \times 3 \times 3$ -unit cells and the resultant lateral displacement was extracted by the method described in Ref. [51], to estimate the Poisson's ratio of the bulk material. The plot in **Fig. 5** indicates that the proposed 3D metamaterial exhibits auxeticity when the chosen geometrical parameters lie in the region above the dashed curve, which corresponds to $\mu = 0$. The Poisson's ratio can be further lowered by decreasing (increasing) the value of d/p (θ) and can reach a minimum of $\mu = -0.28$ for $\theta = 34^\circ$ and $d = 0.06p$.

APPENDIX B: DESCRIPTION OF THE TWO NODES

Most micro-lattice-based metamaterials comprise vertices that are identical and can be described only by one of kind of node, as shown in an illustrative example in **Fig. 6(a)**. The prominent octet-truss lattice [19,42] in **Fig. 6(a)** would therefore possess only one uniform set of natural frequencies. In the metamaterial proposed in this work however, there are two types of nodes as shown in **Fig. 6(b)**. Node 1 is connected to a total of 5 struts (4 inner and 1 outer), while the node 2 is connected only to 2 inner struts.

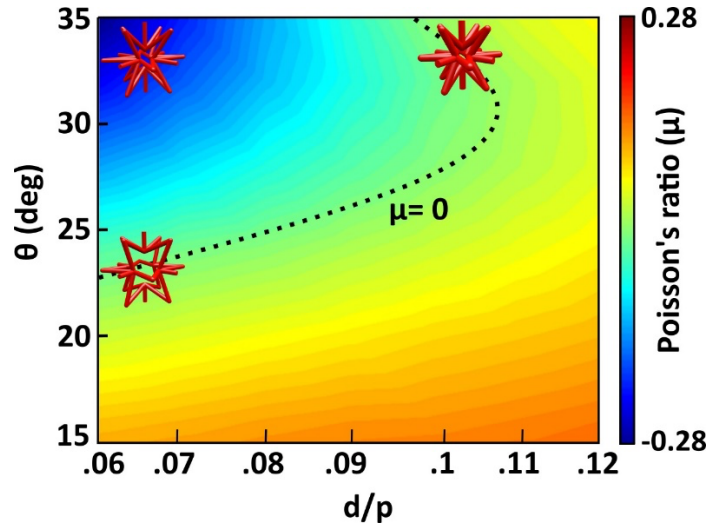


Figure 5. Poisson's ratio, μ , for different values of θ and d/p , when $E = 512$ MPa, $a = 0.8p$, $\nu = 0.3$, $\rho = 1.1$ g/cm³. Insets show the geometry of the unit cell for the larger negative value of μ and for when $\mu = 0$.

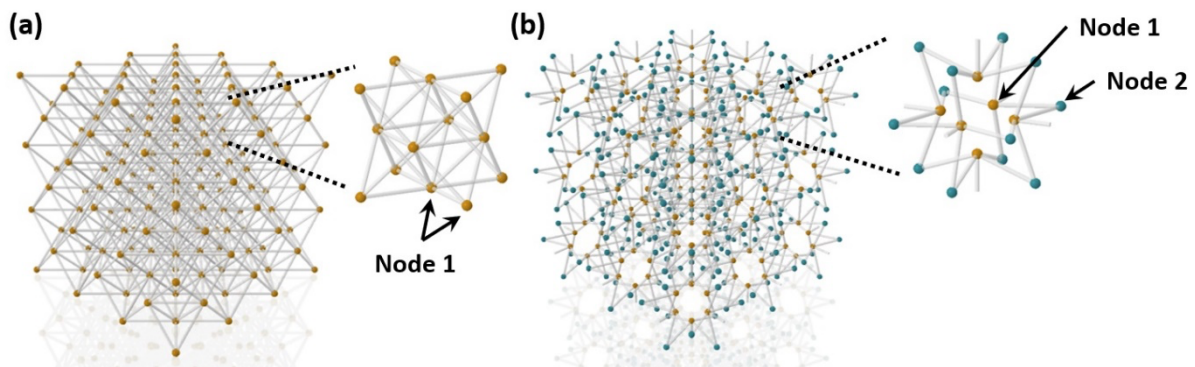


Figure 6. (a) Identical nodes in a conventional octet-truss lattice [19,42]. (b) The two different nodes of the isotaxal auxetic unit cell that is proposed here

APPENDIX C: THEORETICAL MODEL TO EVALUATE MASS AND STIFFNESS

The unit cell of the proposed metamaterial (shown in Fig. 7(a)) can be described as a combination of two different masses and springs, as illustrated in Fig. 7(b). Here mass 2 (m_2) is connected to mass 1 (m_1) through a spring K_2 , and m_1 is in turn connected to the neighboring unit via a spring K_1 . Such a system would therefore possess resonances that arise as a result of m_1 - K_1 as well as m_2 -

K_2 and would thus give rise to the two different BGs that are seen in **Fig. 1(d)**. Since node 1 is connected to 5 struts, the total mass of m_1 , can be obtained by first expressing the effective length of the strut in terms of the angle, θ , shown in **Fig. 7(c)**. the resultant expression for m_2 would therefore be,

$$m_1 = \left(\frac{a}{2\cos\theta} + \frac{p+a(\tan\theta-1)}{8} \right) \rho\pi d^2 \quad (\text{C1})$$

The effective stiffness of the spring, K_1 , can then be evaluated by calculating the total reaction force, F_{t1} , at the node 1 that would impose a unit displacement, δ_1 . F_{t1} can in turn be expressed as the sum of the reaction forces that occur in the vertical strut and the 4 inclined struts that are denoted below by F_{v1} and F_{i1} , respectively. These can be calculated via the expressions for the bending deflection of a simply supported beam and would give,

$$F_{v1} = \frac{E\pi d^2 \delta_1}{2p+2a(\tan\theta-1)} \quad (\text{C2})$$

$$F_{i1} = \frac{E\pi d^2}{a} \left(\frac{3d^2 \cos^5\theta}{8a^2} + \frac{\sin^2\theta \cos\theta}{2} \right) \quad (\text{C3})$$

The effective stiffness of the spring, K_1 , can hence be obtained as,

$$K_1 = \frac{F_{t1}}{\delta_1} = \frac{4F_{i1}+F_{v1}}{\delta_1} \quad (\text{C4})$$

which results in the following expression for the local effective stiffness of node 1,

$$K_1 = \left[\frac{3d^2 \cos^5\theta}{2a^3} + \frac{2\sin^2\theta \cos\theta}{a} + \frac{1}{2p+2a(\tan\theta-1)} \right] E\pi d^2 \quad (\text{C5})$$

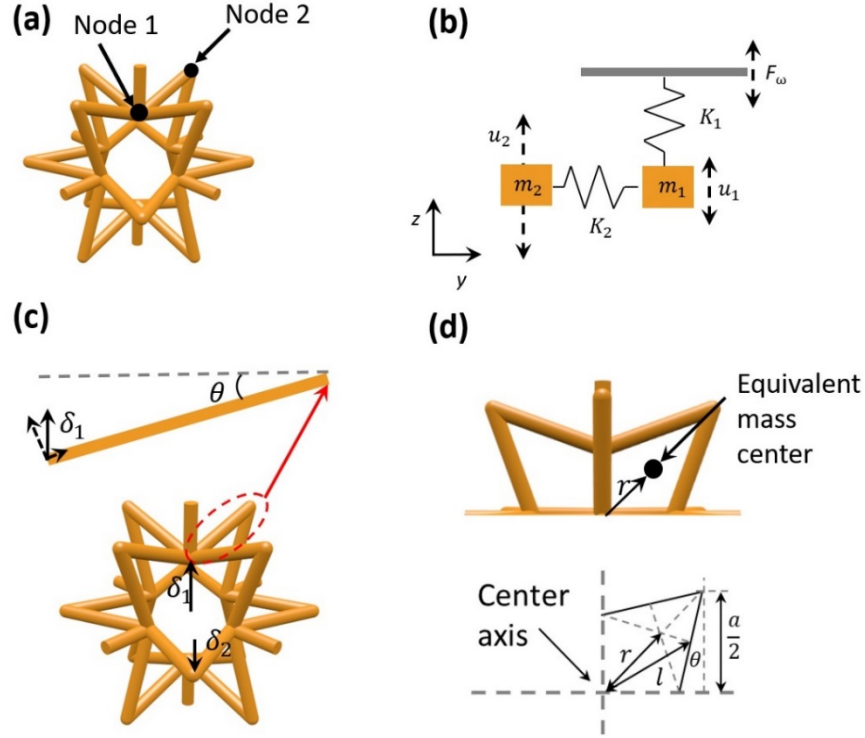


Figure 7. (a) Unit cell of the proposal 3D elastic metamaterial with the 2 nodes described in **Appendix B** (b) shows its equivalent spring-mass system. F_ω is the external excitation, while u_1 and u_2 denote the displacements of the individual masses (c) Bottom shows the isotaxal auxetic unit cell that experiences the displacements, δ_1 and δ_2 at nodes 1 and 2, respectively. Top shows the node 1 attached an inclined strut, with an angle, θ . (d) Top shows the equivalent mass center for the node 2 that is offset from the center axis and bottom indicates the parameters, r , and l , in this context.

Node 2, on the other hand, is modeled as one that possess a torsional spring, since the equivalent mass at node 2, is offset from the central axis by a distance, r , as denoted in **Fig. 7(d)**. As per the parallel axis theorem, the total moment of inertia at this node, J_2 , can be calculated as

$$J_2 = 2J + 2ML^2 \quad (\text{C6})$$

where J refers the moment of inertia of each strut to its centre and M denotes the mass of the strut, both of which can be calculated as,

$$J = \frac{1}{12}ML^2 = \frac{1}{12}\rho\pi\left(\frac{d}{2}\right)^2\left(\frac{a}{2\cos\theta}\right)^3 \quad (\text{C7})$$

$$M = \frac{a}{8\cos\theta} \rho\pi d^2 \quad (\text{C8})$$

where l is the distance from the strut center to the center axis. The torsional stiffness, κ_2 , of the spring at node 2 can then be calculated as done previously, by using the total reaction force, F_{t2} , for the case of a unit displacement, δ_2 , and can be expressed as,

$$\kappa_2 = \frac{F_{t2}r^2}{\delta_2} \quad (\text{C9})$$

F_{t2} in this case can be calculated through the expression,

$$F_{t2} = \frac{48EI\delta_2\cos^3\theta}{a^3} \quad (\text{A10})$$

The distance r can be calculated by,

$$r = \frac{a}{2} \left[\frac{\cos(45^\circ - \theta)}{3\cos\theta} + \frac{\sqrt{2}}{2} (1 - \tan\theta) \right] \quad (\text{C11})$$

The effective stiffness, κ_2 , of the torsional spring would therefore be equivalent to,

$$\kappa_2 = E\pi d^2 \frac{3d^2\cos^3\theta}{a} \left[\frac{\cos(45^\circ - \theta)}{3\cos\theta} + \frac{\sqrt{2}}{2} (1 - \tan\theta) \right]^2 \quad (\text{C12})$$

Lastly, the mass and stiffness of node 2 can be calculated by writing $m_2 = J_2/r^2$ and $K_2 = \kappa_2/r^2$ and would subsequently yield the following expressions,

$$m_2 = \frac{\rho\pi d^2}{16} \left[\frac{a}{3\cos^3\theta} + \frac{a(\tan^2\theta - 4\tan\theta + 5)}{\cos\theta} \right] \left[\frac{\cos(45^\circ - \theta)}{3\cos\theta} + \frac{\sqrt{2}}{2} (1 - \tan\theta) \right]^{-2} \quad (\text{C13})$$

$$K_2 = E\pi d^2 \frac{3d^2\cos^3\theta}{4a^3} \quad (\text{C14})$$

APPENDIX D: EVALUATION OF THE DYNAMIC EFFECTIVE PROPERTIES

The theoretical characterization of the effective parameters is achieved by calculating the average forces, displacement, stress and strain of the unit cell along the boundaries 1-6, shown in **Fig. 8**. The calculations were performed at the X point of the irreducible Brillouin Zone. F_x^{eff} and U_x^{eff} can be obtained by averaging the stress along the boundaries of the unit cell,

$$F_x^{eff} = - \int_1 T_{xx} ds + \int_3 T_{xx} ds - \int_2 T_{xy} ds + \int_4 T_{xy} ds - \int_5 T_{xz} ds + \int_6 T_{xz} ds \quad (D1)$$

$$U_x^{eff} = \frac{1}{2p^2} \left(\int_1 u_x ds + \int_3 u_x ds \right) \quad (D2)$$

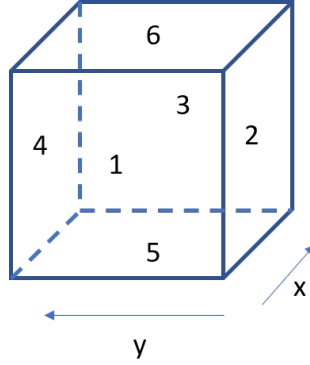


Figure 8. Labeled boundaries 1-6 of the cubic unit cell

Likewise, the components of the effective stress and strain tensors, T_{ij}^{eff} and S_{ij}^{eff} , the effective

elastic constants, C_{ij}^{eff} , can be calculated as,

$$T_{xx}^{eff} = \frac{1}{2p^2} \left(\int_1 T_{xx} ds + \int_3 T_{xx} ds \right),$$

$$T_{yy}^{eff} = \frac{1}{2p^2} \left(\int_2 T_{yy} ds + \int_4 T_{yy} ds \right),$$

$$T_{zz}^{eff} = \frac{1}{2p^2} \left(\int_5 T_{zz} ds + \int_6 T_{zz} ds \right),$$

$$T_{xy}^{eff} = \frac{1}{2p^2} \left(\int_2 T_{xy} ds + \int_4 T_{xy} ds \right)$$

$$S_{xx}^{eff} = \frac{1}{p^3} \left(\int_3 u_x ds - \int_1 u_x ds \right),$$

$$S_{yy}^{eff} = \frac{1}{p^3} \left(\int_4 u_y ds - \int_2 u_y ds \right),$$

$$S_{zz}^{eff} = \frac{1}{p^3} \left(\int_6 u_y ds - \int_5 u_y ds \right),$$

$$S_{xy}^{eff} = \frac{1}{2p^3} \left(\int_4 u_x ds - \int_2 u_x ds \right) + \frac{1}{2p^3} \left(\int_3 u_y ds - \int_1 u_y ds \right) \quad (D3)$$

The stress-strain matrix for a three-dimensional cubic unit cell can be written as [47],

$$\begin{pmatrix} T_{xx}^{eff} \\ T_{yy}^{eff} \\ T_{zz}^{eff} \\ T_{yz}^{eff} \\ T_{xz}^{eff} \\ T_{xy}^{eff} \end{pmatrix} = \begin{pmatrix} C_{11}^{eff} & C_{12}^{eff} & C_{12}^{eff} & 0 & 0 & 0 \\ C_{11}^{eff} & C_{11}^{eff} & C_{12}^{eff} & 0 & 0 & 0 \\ C_{12}^{eff} & C_{12}^{eff} & C_{11}^{eff} & 0 & 0 & 0 \\ 0 & 0 & 0 & C_{44}^{eff} & 0 & 0 \\ 0 & 0 & 0 & 0 & C_{44}^{eff} & 0 \\ 0 & 0 & 0 & 0 & 0 & C_{44}^{eff} \end{pmatrix} \begin{pmatrix} S_{xx}^{eff} \\ S_{yy}^{eff} \\ S_{zz}^{eff} \\ 2S_{yz}^{eff} \\ 2S_{xz}^{eff} \\ 2S_{xy}^{eff} \end{pmatrix} \quad (D4)$$

where T_{ij}^{eff} , and S_{ij}^{eff} are the components of the effective stress and strain tensors respectively,

with i and j representing the different directions of propagation, i.e., $i \in \{x, y, z\}$. These stress and

strain values were calculated for each frequency as per the method described above and employed

to compute the effective elastic constants, C_{ij}^{eff} . The effective bulk modulus was then obtained

using the expression,

$$\kappa_{eff} = \frac{C_{11}^{eff} + C_{12}^{eff}}{2} \quad (D5)$$

Likewise, the effective density, ρ_{eff} , was calculated through the Newton's Second Law, by the

following expression [46],

$$\begin{pmatrix} F_x^{eff} \\ F_y^{eff} \\ F_z^{eff} \end{pmatrix} = \begin{pmatrix} \rho_{xx}^{eff} & \rho_{xy}^{eff} & \rho_{xz}^{eff} \\ \rho_{yx}^{eff} & \rho_{yy}^{eff} & \rho_{yz}^{eff} \\ \rho_{zx}^{eff} & \rho_{zy}^{eff} & \rho_{zz}^{eff} \end{pmatrix} \begin{pmatrix} U_x^{eff} \\ U_y^{eff} \\ U_z^{eff} \end{pmatrix} \quad (D6)$$

where F_i^{eff} and U_i^{eff} , refer to the effective forces exerted and the resultant displacements along

the i^{th} direction of the unit cell and can be calculated through **Eqns. D1** and **D2**. Since the excitation

here is purely longitudinal, this study is focused on extracting the effective properties only for the

longitudinal mode thereby focusing only on the diagonal terms of the matrix in **Eqn. D6**. Additionally, due to the cubic symmetry, the diagonal terms of the effective density matrix would be equal, i.e., $\rho_{xx}^{eff} = \rho_{yy}^{eff} = \rho_{zz}^{eff}$, and would hence further reduce **Eqn. D6** to,

$$\rho_{eff} = -\frac{F^{eff}}{\omega^2 p^3 U^{eff}} \quad (\text{D7})$$

APPENDIX E: SAMPLE FABRICATION

The fabrication of our intricate isotaxal based elastic metamaterial was made possible by a high-resolution, large area projection micro-stereolithography (LAP μ SL) platform that utilized a layer-by-layer digital light manufacturing technique, as shown in **Fig. 9(a)**. LAP μ SL [19,42,52] is capable of fabricating complex structures with feature sizes ranging from microns to a few centimeters. Firstly, in order to enable the printability of the lattice, supports (that can later be removed or dissolved) were added at the overhanging positions. The three-dimensional CAD model of the sample was then sliced into a group of two-dimensional images, which were subsequently transmitted to a digital micro-mirror device (DMD) chip. The UV light from the diode array was patterned by the modulator and then transmitted through a lens system to reduce the pattern size and to increase the resolution. The patterned UV light was then projected onto the surface of a UV-curable resin to form the shape of the 2D slice on a printing substrate. After the curing of the first layer, the printing substrate was lowered for the re-coating of the liquid resin and the process was repeated until the formation of the whole 3D micro-lattice. The scalability of the fabrication system was expanded by coordinating the projection set-up with an optical scanning system, which allowed the UV pattern to be exposed to different areas within a single layer. After printing, the samples were cleaned with ethanol, the internal supports were removed, and then post-cured under UV light. The material employed here is composed of a polymer (1,6 –

Hexanediol diacrylate), photo-initiator (phenylbis (2,4,6-trimethylbenzoyl) phosphine oxide), and photo-absorber (Sudan 1). The material properties of this resin were consistent with the values incorporated in the numerical simulation (Young's Modulus, $E = 512$ MPa; density, $\rho = 1.1$ g/cm³; intrinsic Poisson's ratio, $\nu = 0.3$).

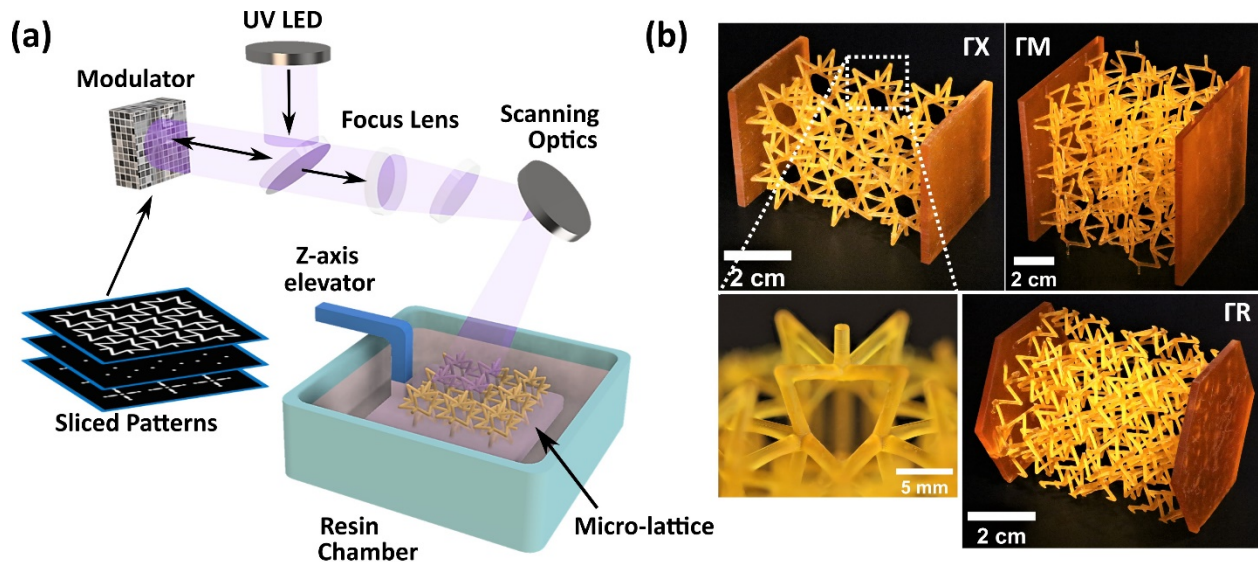


Figure 9. (a) Schematic illustration of the fabrication technique. (b) Photographs of the ultra-light isotoxal star-based metamaterial samples, fabricated in the ΓX (top left), ΓM (top right) and ΓR (bottom right) directions, with the same unit cell dimensions and with period, $p = 2$ cm. Bottom left shows a close-up optical image of the ΓX sample, featuring the overhanging structure in the present metamaterial.

APPENDIX F: CORRECTED BANDSTRUCTURE FOR THE EXPERIMENTALLY MEASURED SAMPLES

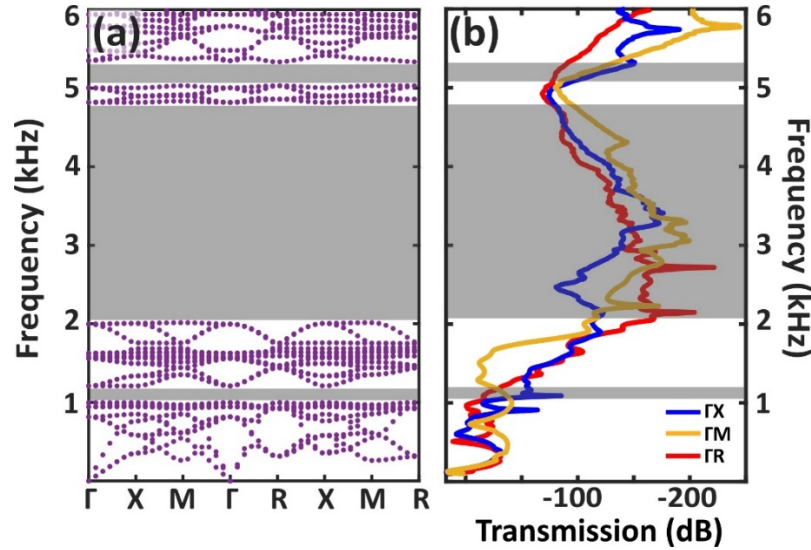


Figure 10. (a) Complete bandstructure for a sample of dimensions, $p = 2$ cm, $a = 1.6$ cm, $d = 1.2$ mm, $\theta = 21^\circ$, and material properties, $E = 415$ MPa, $\nu = 0.3$ and $\rho = 1.1$ g/cm³. (b) Measurement results for frequency dependent transmission, for samples along the ΓX , ΓM and ΓR directions, also shown in Fig. 4(h).

APPENDIX G: HYBRID METAMATERIAL SAMPLE WITH AN EXTREMELY WIDE BANDGAP

The hybrid sample can be made possible by combining three pairs of unit cells with different but overlapping bandgaps. Here, the three-unit cells chosen had the same θ value but different d values. The values of d were chosen from the bandgap analysis, that is shown in Fig. 2(a) of the main text. At first, the transmission performance for each of the cases were examined when only two-unit cells were considered. Fig. 11(a) here, shows the transmission results for $d = 0.06p$, $0.08p$ and $0.10p$, which are denoted by the red, blue, and green curves, respectively. High attenuation of the wave is clearly seen in the desired frequency ranges for each of the cases: $f \cdot p$ from 46 to 111 for $d = 0.06p$; from 68.2 to 150.8, for $d = 0.08p$ and from 90 to 184, for $d =$

$0.10p$. The three units were then combined and the wave transmission through this hybrid design can be seen in **Fig. 11(b)**. An overall attenuation can be seen in the frequency ranges of the three individual bandgaps seen in **Fig. 11(a)**. **Fig. 11(c)**, shows the normalized displacement field amplitude for the hybrid micro-lattice along its ΓX direction, at the frequencies indicated by (1) inside the first bandgap but outside the second, (2) inside the common the regions of the three bandgaps, (3) inside the second and the third bandgap and (4), inside the third bandgap, but outside the others. The waves of frequencies (1) and (2) are completely attenuated by the first two-unit cells (which correspond to $d = 0.06p$). Higher attenuation is seen in (2) since the wave at this frequency does not propagate through any of the units. In the case of (3), the wave propagates through the first two units and then gets completely attenuated by the unit cells that correspond to $d = 0.08a$ and $d = 0.10p$, since its frequency lies in the overlapping region of the bandgaps of $d = 0.08a$ and $d = 0.10p$. Finally, for the frequency indicated by (4), the wave propagates through the first 4 units, since it is no longer in the bandgap region associated with $d = 0.06p$ and $d = 0.08p$, but it gets completely reflected by the two units that correspond to $d = 0.10p$. For $p = 2$ cm, this hybrid sample would only be 6.5cm in thickness but will facilitate an ultra-wide bandgap of width 130%.

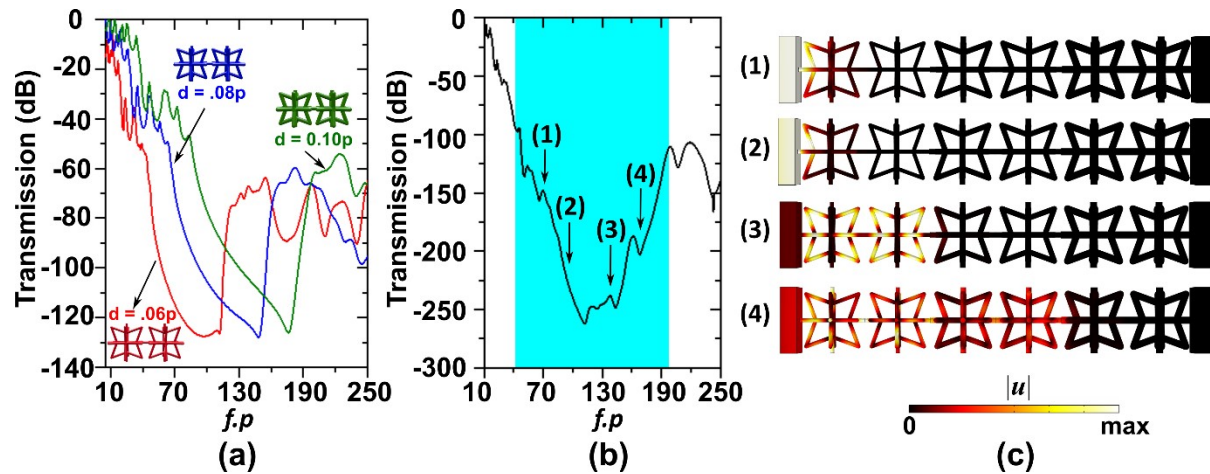


Figure 11. (a) Transmission (dB), through two-unit cells for the cases of $d = 0.06p$, $d = 0.08p$ and $d = 0.10p$. (b) Elastic wave transmission in the ΓX directions, through the hybrid sample made up of the three sets of unit cells. (c) Normalized displacement field amplitude through the sample for the four different frequencies that are indicated in the transmission spectrum in (b).

REFERENCES

- [1] S. A. Cummer, J. Christensen, and A. Alù, *Controlling Sound with Acoustic Metamaterials*, Nat. Rev. Mater. **1**, 16001 (2016).
- [2] H. Ge, M. Yang, C. Ma, M.-H. Lu, Y.-F. Chen, N. Fang, and P. Sheng, *Breaking the Barriers: Advances in Acoustic Functional Materials*, Natl. Sci. Rev. **5**, 159 (2018).
- [3] Y. Jin, Y. Pennec, B. Bonello, H. Honarvar, L. Dobrzynski, B. Djafari-Rouhani, and M. I. Hussein, *Physics of Surface Vibrational Resonances: Pillared Phononic Crystals, Metamaterials, and Metasurfaces*, Rep. Prog. Phys. (2021).
- [4] M. I. Hussein, M. J. Leamy, and M. Ruzzene, *Dynamics of Phononic Materials and Structures: Historical Origins, Recent Progress, and Future Outlook*, Appl. Mech. Rev. **66**, 040802 (2014).
- [5] M. Oudich, Y. Li, B. M. Assouar, and Z. Hou, *A Sonic Band Gap Based on the Locally Resonant Phononic Plates with Stubs*, New J. Phys. **12**, 083049 (2010).
- [6] F. Warmuth, M. Wormser, and C. Körner, *Single Phase 3D Phononic Band Gap Material*, Sci. Rep. **7**, 3843 (2017).
- [7] O. McGee, H. Jiang, F. Qian, Z. Jia, L. Wang, H. Meng, D. Chronopoulos, Y. Chen, and L. Zuo, *3D Printed Architected Hollow Sphere Foams with Low-Frequency Phononic Band Gaps*, Addit. Manuf. **30**, 100842 (2019).
- [8] X. Fei, L. Jin, X. Zhang, X. Li, and M. Lu, *Three-Dimensional Anti-Chiral Auxetic Metamaterial with Tunable Phononic Bandgap*, Appl. Phys. Lett. **116**, 021902 (2020).
- [9] F. Lucklum and M. J. Vellekoop, *Bandgap Engineering of Three-Dimensional Phononic Crystals in a Simple Cubic Lattice*, Appl. Phys. Lett. **113**, 201902 (2018).
- [10] X. An, C. Lai, W. He, and H. Fan, *Three-Dimensional Meta-Truss Lattice Composite Structures with Vibration Isolation Performance*, Extreme Mech. Lett. **33**, 100577 (2019).
- [11] S. Taniker and C. Yilmaz, *Design, Analysis and Experimental Investigation of Three-Dimensional Structures with Inertial Amplification Induced Vibration Stop Bands*, Int. J. Solids Struct. **72**, 88 (2015).

- [12] K. H. Matlack, A. Bauhofer, S. Krödel, A. Palermo, and C. Daraio, *Composite 3D-Printed Metastructures for Low-Frequency and Broadband Vibration Absorption*, Proc. Natl. Acad. Sci. U. S. A. **113**, 8386 (2016).
- [13] W. Elmadih, D. Chronopoulos, W. P. Syam, I. Maskery, H. Meng, and R. K. Leach, *Three-Dimensional Resonating Metamaterials for Low-Frequency Vibration Attenuation*, Sci. Rep. **9**, 11503 (2019).
- [14] O. R. Bilal, D. Ballagi, and C. Daraio, *Architected Lattices for Simultaneous Broadband Attenuation of Airborne Sound and Mechanical Vibrations in All Directions*, Phys. Rev. Appl. **10**, 054060 (2018).
- [15] L. D'Alessandro, E. Belloni, R. Ardito, F. Braghin, and A. Corigliano, *Mechanical Low-Frequency Filter via Modes Separation in 3D Periodic Structures*, Appl. Phys. Lett. **111**, 231902 (2017)
- [16] O. R. Bilal, A. Foehr, and C. Daraio, *Observation of Trampoline Phenomena in 3D-Printed Metamaterial Plates*, Extreme Mech. Lett. **15**, 103 (2017).
- [17] O. R. Bilal and M. I. Hussein, *Trampoline Metamaterial: Local Resonance Enhancement by Springboards*, Appl. Phys. Lett. **103**, 111901 (2013).
- [18] Y. Jin, Y. Pennec, Y. Pan, and B. Djafari-Rouhani, *Phononic Crystal Plate with Hollow Pillars Connected by Thin Bars*, J. Phys. Appl. Phys. **50**, 035301 (2016).
- [19] X. Zheng, H. Lee, T. H. Weisgraber, M. Shusteff, J. DeOtte, E. B. Duoss, J. D. Kuntz, M. M. Biener, Q. Ge, J. A. Jackson, S. O. Kucheyev, N. X. Fang, and C. M. Spadaccini, *Ultralight, Ultrastiff Mechanical Metamaterials*, Science **344**, 1373 (2014).
- [20] A. Torrents, T. A. Schaedler, A. J. Jacobsen, W. B. Carter, and L. Valdevit, *Characterization of Nickel-Based Microlattice Materials with Structural Hierarchy from the Nanometer to the Millimeter Scale*, Acta Mater. **60**, 3511 (2012).
- [21] Q. Wang, J. A. Jackson, Q. Ge, J. B. Hopkins, C. M. Spadaccini, and N. X. Fang, *Lightweight Mechanical Metamaterials with Tunable Negative Thermal Expansion*, Phys. Rev. Lett. **117**, 175901 (2016).
- [22] T. A. Schaedler, C. J. Ro, A. E. Sorensen, Z. Eckel, S. S. Yang, W. B. Carter, and A. J. Jacobsen, *Designing Metallic Microlattices for Energy Absorber Applications*, Adv. Eng. Mater. **16**, 276 (2014).
- [23] C. S. Ha, R. S. Lakes, and M. E. Plesha, *Cubic Negative Stiffness Lattice Structure for Energy Absorption: Numerical and Experimental Studies*, Int. J. Solids Struct. **178–179**, 127 (2019).
- [24] M. Kadic, G. W. Milton, M. van Hecke, and M. Wegener, *3D Metamaterials*, Nat. Rev. Phys. **1**, 198 (2019).
- [25] L. Cabras and M. Brun, *A Class of Auxetic Three-Dimensional Lattices*, J. Mech. Phys. Solids **91**, 56 (2016).
- [26] X. Ren, R. Das, P. Tran, T. D. Ngo, and Y. M. Xie, *Auxetic Metamaterials and Structures: A Review*, Smart Mater. Struct. **27**, 023001 (2018).
- [27] R. Lakes, *Foam Structures with a Negative Poisson's Ratio*, Science **235**, 1038 (1987).
- [28] M. Mir, M. N. Ali, J. Sami, and U. Ansari, *Review of Mechanics and Applications of Auxetic Structures*, Adv. Mater. Sci. Eng. **2014**, e753496 (2014).
- [29] A. Spadoni, *An Isotropic Auxetic Structural Network With Limited Shear Stiffness*, in (American Society of Mechanical Engineers Digital Collection, 2012), pp. 179–187.
- [30] J. Dirrenberger, S. Forest, and D. Jeulin, *Effective Elastic Properties of Auxetic Microstructures: Anisotropy and Structural Applications*, Int. J. Mech. Mater. Des. **9**, 21 (2013).
- [31] C. S. Ha, M. E. Plesha, and R. S. Lakes, *Chiral Three-Dimensional Isotropic Lattices with Negative Poisson's Ratio*, Phys. Status Solidi B **253**, 1243 (2016).
- [32] J. N. Grima and K. E. Evans, *Auxetic Behavior from Rotating Squares*, J. Mater. Sci. Lett. **19**, 1563 (2000).
- [33] D. Attard and J. N. Grima, *Auxetic Behaviour from Rotating Rhombi*, Phys. Status Solidi B **245**, 2395 (2008).
- [34] J. N. Grima, L. Mizzi, K. M. Azzopardi, and R. Gatt, *Auxetic Perforated Mechanical Metamaterials with Randomly Oriented Cuts*, Adv. Mater. **28**, 385 (2016).

- [35] J. Meng, Z. Deng, K. Zhang, X. Xu, and F. Wen, *Band Gap Analysis of Star-Shaped Honeycombs with Varied Poisson's Ratio*, Smart Mater. Struct. **24**, 095011 (2015).
- [36] A. Bacigalupo, M. Lepidi, G. Gnecco, and L. Gambarotta, *Optimal Design of Auxetic Hexachiral Metamaterials with Local Resonators*, Smart Mater. Struct. **25**, 054009 (2016).
- [37] S. Mukherjee, Fabrizio Scarpa, and S. Gopalakrishnan, *Phononic Band Gap Design in Honeycomb Lattice with Combinations of Auxetic and Conventional Core*, Smart Mater. Struct. **25**, 054011 (2016).
- [38] L. D'Alessandro, V. Zega, R. Ardito, and A. Corigliano, *3D Auxetic Single Material Periodic Structure with Ultra-Wide Tunable Bandgap*, Sci. Rep. **8**, 2262 (2018).
- [39] S. Krödel, T. Delpero, A. Bergamini, P. Ermanni, and D. M. Kochmann, *3D Auxetic Microlattices with Independently Controllable Acoustic Band Gaps and Quasi-Static Elastic Moduli*, Adv. Eng. Mater. **16**, 357 (2014).
- [40] C. R. de Lima and G. H. Paulino, *Auxetic Structure Design Using Compliant Mechanisms: A Topology Optimization Approach with Polygonal Finite Elements*, Adv. Eng. Softw. **129**, 69 (2019).
- [41] T. A. Schaedler, A. J. Jacobsen, A. Torrents, A. E. Sorensen, J. Lian, J. R. Greer, L. Valdevit, and W. B. Carter, *Ultralight Metallic Microlattices*, Science **334**, 962 (2011).
- [42] X. Zheng, W. Smith, J. Jackson, B. Moran, H. Cui, D. Chen, J. Ye, N. Fang, N. Rodriguez, T. Weisgraber, and C. M. Spadaccini, *Multiscale Metallic Metamaterials*, Nat. Mater. **15**, 1100 (2016).
- [43] A. O. Krushynska, A. Amendola, F. Bosia, C. Daraio, N. M. Pugno, and F. Fraternali, *Accordion-like Metamaterials with Tunable Ultra-Wide Low-Frequency Band Gaps*, New J. Phys. **20**, 073051 (2018).
- [44] Y. Chen and L. Wang, *Periodic Co-Continuous Acoustic Metamaterials with Overlapping Locally Resonant and Bragg Band Gaps*, Appl. Phys. Lett. **105**, 191907 (2014).
- [45] L. D'Alessandro, E. Belloni, R. Ardito, A. Corigliano, and F. Braghin, *Modeling and Experimental Verification of an Ultra-Wide Bandgap in 3D Phononic Crystal*, Appl. Phys. Lett. **109**, 221907 (2016).
- [46] M. Oudich, B. Djafari-Rouhani, Y. Pennec, M. B. Assouar, and B. Bonello, *Negative Effective Mass Density of Acoustic Metamaterial Plate Decorated with Low Frequency Resonant Pillars*, J. Appl. Phys. **116**, 184504 (2014).
- [47] Y. Lai, Y. Wu, P. Sheng, and Z.-Q. Zhang, *Hybrid Elastic Solids*, Nat. Mater. **10**, 620 (2011).
- [48] X. Zhang and Z. Liu, *Negative Refraction of Acoustic Waves in Two-Dimensional Phononic Crystals*, Appl. Phys. Lett. **85**, 341 (2004).
- [49] X. Zhou, M. B. Assouar, and M. Oudich, *Acoustic Superfocusing by Solid Phononic Crystals*, Appl. Phys. Lett. **105**, 233506 (2014).
- [50] D. Chen and X. Zheng, *Multi-Material Additive Manufacturing of Metamaterials with Giant, Tailorable Negative Poisson's Ratios*, Sci. Rep. **8**, 9139 (2018).
- [51] G. Imbalzano, P. Tran, T. D. Ngo, and P. V. Lee, *Three-Dimensional Modelling of Auxetic Sandwich Panels for Localised Impact Resistance*, J. Sandw. Struct. Mater. **19**, 291 (2017).
- [52] N. J. Gerard, H. Cui, C. Shen, Y. Xie, S. Cummer, X. Zheng, and Y. Jing, *Fabrication and Experimental Demonstration of a Hybrid Resonant Acoustic Gradient Index Metasurface at 40 KHz*, Appl. Phys. Lett. **114**, 231902 (2019).
- [53] See Supplemental Material at [URL will be inserted by published] for [give brief description of material].